MORPHOLOGICAL SLOPE FAILURE DETECTION USING MULTISENSOR DATA MERGED BY WAVELET TRANSFORM

Makoto KAWAMURA*, Kazuhiko TSUJINO, Yuji TSUJIKO*****
*Toyohashi University of Technology, Japan
Department of Architecture and Civil Engineering
kawamura@acserv.tutrp.tut.ac.jp
**Fukui National College of Technology, Japan
Department of Civil Engineering
tsujino@be.fukui-nct.ac.jp
***Fukui National College of Technology, Japan
Department of Civil Engineering
tsujiko@be.fukui-nct.ac.jp

Working Group IC-24

KEY WORDS: Slope Failure, Landslide, Mathematical Morphology, Wavelet Transform, Multi-sensor Data.

ABSTRACT

This paper describes a slope failure detector based on mathematical morphological operations. Multi-sensor data, LANDSAT TM, ADEOS AVNIR, SPOT HRV-XS and SPOT HRV-Panchromatic, are chosen as the original images. The proposed detector consists of morphological fundamental operation such as dilation and erosion. The formula was applied to the detection of earthquake-induced slope failures in Rokkko Mountain side triggered by the Hyogoken-Nambu earthquake. The results lead two major conclusions as follows;

(1) The accuracy of proposed slope failure detector depends on the resolution and high-resolution data made by wavelet transform is effective for the input data. Best result of proposed method showed almost perfect for failures of over 1000 m^2.
(2) The accuracy of detection depends on the band (wavelength) of the input data rather than the resolution.

1 INTRODUCTION

Many slope failures in Rokko mountain side were triggered by the Hyogoken-Nambu earthquake, Jan. 17th 1995, along several active faults. Okimura et al.(1995) and Sassa et al.(1996) have surveyed and found hundreds of earthquake-induced slope failures and landslides after the earthquake. The failures were almost linearly distributed along the line of aftershocks. Most of them showed limited motion probably affected by less saturated soil(decomposed granite) due to very dry season.

Such decomposed granites are covering Rokko area so that it is easy to be caused landslides or slope failures in the area by earthquake or heavy rainfall. To prevent the secondary damage for this type of the area, it is necessary to detect the initially collapsed area immediately after the earthquake and to predict/make hazard maps as to secondary damage caused by earthquakes or rainfall.

Authors have already proposed a morphological edge detector for hazard mapping(Kawamura,1994, 1996) and also have proposed a morphological slope failure detector. The detector has applied to the satellite data covering Hyogoken-Nambu area, Japan(Kawamura et al.1995). Structuring elements used in the morphological function are given by computing the relationship between the CCT count(digital number, DN) and the land cover condition. This detector outputs the failure type(dropping or sliding), the size of the failure and the shape of the failure by subtracting two temporal satellite imageries.

To give the accurate outputs the proposed detector, however, requires high-resolution daily data. Unfortunately it is difficult to acquire such data with the present situation. In this study we tried to make such high-resolution data from low-resolution data by wavelet transform. Five case studies are prepared corresponding to the input data. The results are compared using mesh diagram and percent total accuracies.

2 SATELLITE DATA USED IN THIS STUDY

2.1 Original Data

Table 1 shows data and its descriptions used in this study. Pair images of both before and after the Hyogoken-Nambu earthquake for each sensor, except ADEOS, are prepared. Figure 1 is the SPOT HRV-XS image of study site.

Data	Descriptions						
	Platform	Sensor	Path	Row	Date	Image size	Resolution
Before The Hyogo-ken Nambu Earthquake	LANDSAT	TM	110	36	Mar.23.1993	695*559	about 30m
	SPOT	HRV-XS	322	280	Oct.23.1991	997*802	about 20m
	SPOT	HRV-Pan	322	280	Oct.23.1991	1994*1604	about 10m
After The Hyogo-ken Nambu Earthquake	LANDSAT	TM	110	36	Jan.24.1995	695*559	about 30m
	SPOT	HRV-XS	322	280	Feb.11.1995	997*802	about 20m
	SPOT	HRV-Pan	322	280	Feb.11.1995	1994*1604	about 10m
	ADEOS	AVNIR	1355	345	Dec.30.1996	1246*1002	about 16m

Table 1. Data used in this study

At the first step, spectral characteristics of bare soils and slope failure area were surveyed. The examples of the result are shown in Figure 2. In 7 bands among LANDSAT TM, DNs of band 5 and band 3 is effective separate into vegetation area and slope failure area (Kawamura et al., 1997). SPOT HRV-XS has no band similar to TM band 5, but HRV-XS band 3 is the data of similar wavelength of LANDSAT TM band 3. Finally, LANDSAT TM band 5, ADEOS AVNIR-Multi band 4 and SPOT HRV-XS band 3 are chosen for the analysis and the comparison.

2.2 Data Merged by Wavelet Transform

Multi-resolution wavelet decomposition and synthesis have been investigated by many researchers(Garguet et al., 1996, Yocky, 1996.) Generally discrete wavelet transform for image decomposition or image synthesis requires the generating function $f_j[k]$ and the scale function $e_j[k]$ as follows;

$$f_j[k]=\frac{1}{2}\left(f_{j+1}[2k]+f_{j+1}[2k+1]\right) \quad (1)$$

$$e_j[k]=\frac{1}{2}\left(f_{j+1}[2k]-f_{j+1}[2k+1]\right). \quad (2)$$

Harr function is used for $f_j[k]$ and $e_j[k]$ in this study. $G(z)$ and $H(z)$ are used as mirror filters assisting of $f_j[k]$ and $e_j[k]$. The $G(z)$ filter associated with $e_j[k]$ is a LPF(Low Pass Filter), while the $H(z)$ filter which as associated with the

Figure 1. Study area (Hyogo-ken, Japan)
(SPOT HRV-XS band 3)

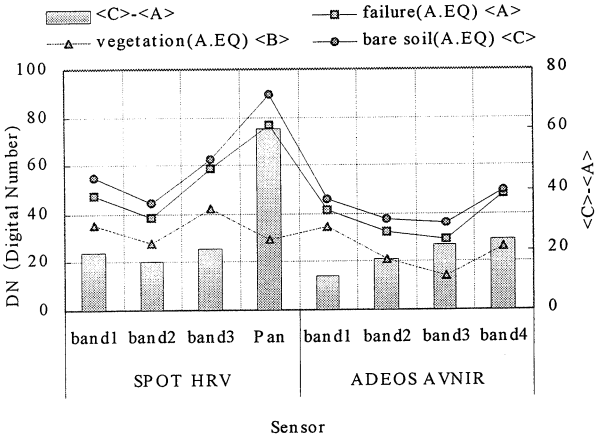

Figure 2. Average DN for study site
A.EQ: after the Hyogoken-Nambu earthquake

wavelet is a HPF(High Pass Filter). The $G(z)$ filter and the $H(z)$ filter are written as follows;

$$G(z)=\frac{1+z}{2} \quad , \quad H(z)=\frac{1-z}{2}. \qquad (3)$$

The $G(z)$ filter and the $H(z)$ filter are used for decomposition. The synthesis filters $P(z)$ and $Q(z)$ corresponding to $G(z)$ and $H(z)$ are shown as follows;

$$P(z)=1+z^{-1} \quad , \quad Q(z)=1-z^{-1} \qquad (4)$$

where z is the coordinate after Z transform and z^{-1} is the delay element.

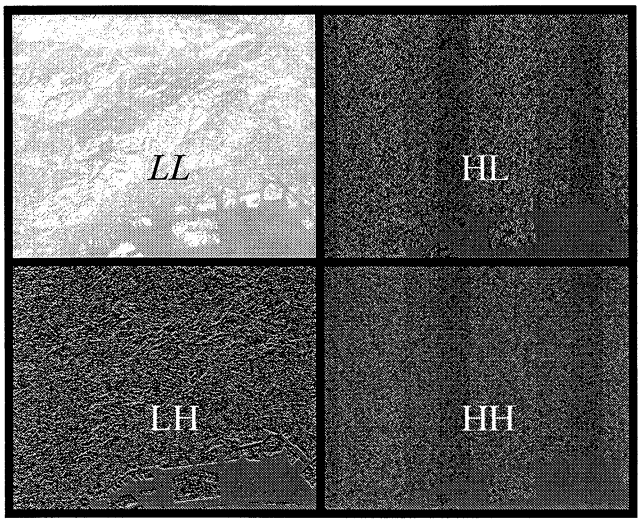

Figure 3. Examples of wavelet decomposition (SPOT HRV-XS band 3)

Figure 3 shows the examples of wavelet decomposition for SPOT-XS band 3. After the decomposition the decomposed data was synthesized with high-resolution data(SPOT HRV-Panchromatic image in this study). Figure 4 shows the parts of original and merged images. 10-m TM and 10m-HRV suggest wavelet transformed images by SPOT HRV-Panchromatic data respectively.

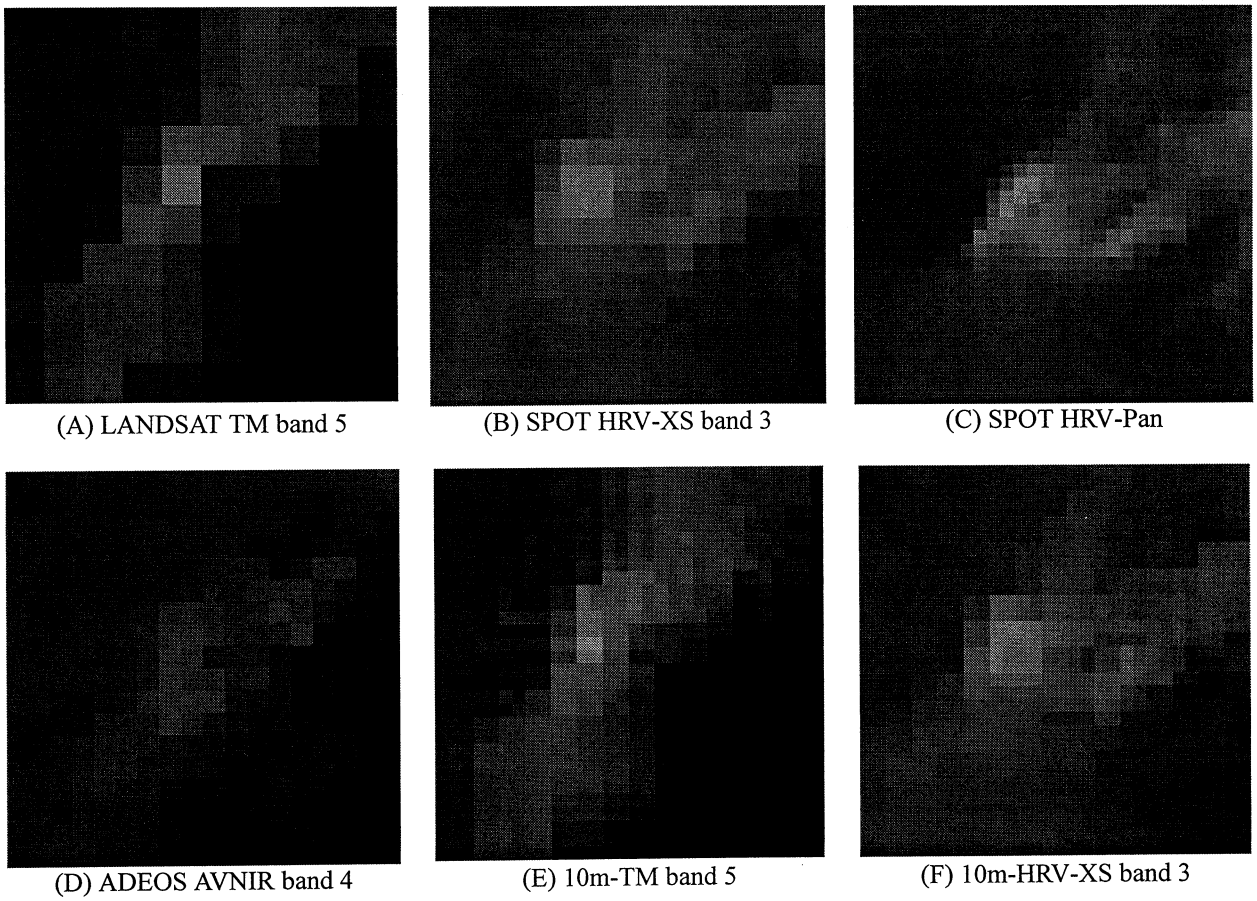

(A) LANDSAT TM band 5 (B) SPOT HRV-XS band 3 (C) SPOT HRV-Pan

(D) ADEOS AVNIR band 4 (E) 10m-TM band 5 (F) 10m-HRV-XS band 3

Figure 4. Comparison of images used in this study (magnified image of same part in the study area)

3 MORPHOLOGICAL SLOPE FAILURE DETECTOR

3.1 Morphological Fundamental Operation

For grayscale image $f(x,y)$, where x, y are coordinates of the image, let original image $f: F \to E$ and structuring element $k: K \to E$. Then dilation $d(x,y)$ ($f \oplus k: F \oplus K \to E$) and erosion $e(x,y)$ can be computed by

$$d(x,y) = \max_{\substack{q \in K, x-q \in F \\ r \in K, y-r \in F}} \{f(x-q, y-r) + k(q,r)\}. \tag{5}$$

$$e(x,y) = \max_{\substack{q \in K, x+q \in F \\ r \in K, y+r \in F}} \{f(x+q, y+r) - k(q,r)\}. \tag{6}$$

By using the outputs of dilation($d: Dil \to E$) and erosion($e: Ero \to E$), morphological opening $o(x,y)$ and closing $c(x,y)$ can be computed as follows;

$$o(x,y) = \max_{\substack{q \in K, x-q \in Ero \\ r \in K, y-r \in Ero}} \{e(x-q, y-r) + k(q,r)\} \tag{7}$$

$$c(x,y) = \max_{\substack{q \in K, x+q \in Dil \\ r \in K, y+r \in Dil}} \{d(x+q, y+r) - k(q,r)\}. \tag{8}$$

3.2 Morphological Slope Failure Operation

Morphological slope failure detector is formulated as;

$$S(x,y) = Go(x,y) - G(x,y) + A(x,y) \tag{9}$$

where $Go(x,y)$ is calculated by opening of $G(x,y)$ with structuring element $K(x,y)$. $G(x,y)$ covers $n \times n$ size of original image where the center pixel is the highest value in the $n \times n$ pixels. $K(x,y)$ is computed using distribution relationship between the digital number and the distance from center pixel as shown Figure 5. $K(x,y)$ also corresponds to center pixel value of $G(x,y)$. $A(x,y)$ is an offset mask that it lets center pixel value be $S(x,y)$.

Morphology of the detected slope failure can be computed by judging the magnitude of $S(x,y)$. Before the judgment, threshold value, $P_1(x,y)$ and $P_2(x,y)$ have to be determined. If $S(x,y)$ is larger than $P_1(x,y)$, then the morphological type of failure is determined as "dropping". If the case of $P_1(x,y) > S(x,y) > P_2(x,y)$, then the type is determined as "sliding". Other case, eg. $S(x,y) < P_2(x,y)$, can be considered as very big failure, so it has to be recalculated by expanding the structuring element size n.

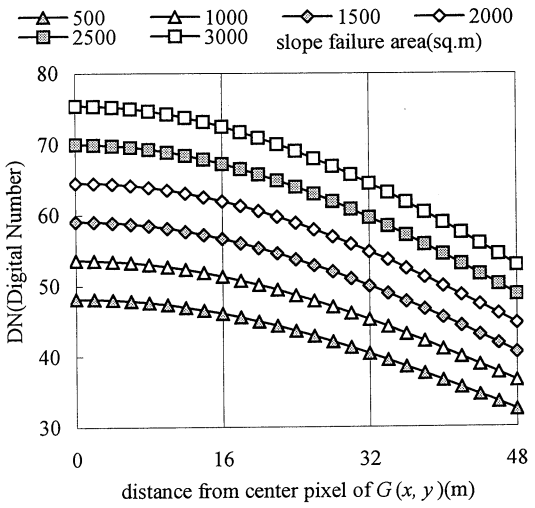

Figure 5. Relationship between digital number and distance from center pixel of $G(x, y)$ (in case of ADEOS AVNIR band 4)

Actual failure **Black: slope failure**	**<Case A>** **TM band 5**	**<Case B>** **HRV-XS band 3**	**<Case C>** **AVNIR band 4**	**<Case D>** **10m-TM band 5**	**<Case E>** **10m-HRV-XSband3**
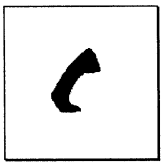	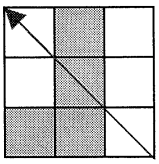	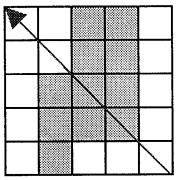	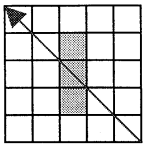	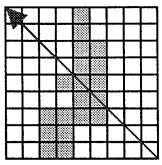	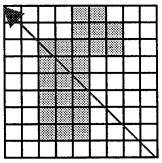
AMF : dropping AAF : 2300m^2	EMF : dropping EAF : 2100m^2	EMF : dropping EAF : 2210m^2	EMF : dropping EAF : 1580m^2	EMF : dropping EAF : 2210m^2	EMF : dropping EAF : 2480m^2
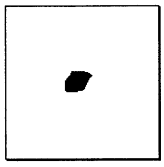	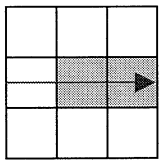	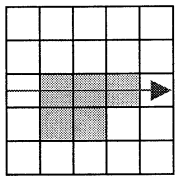	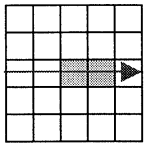	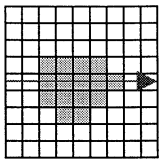	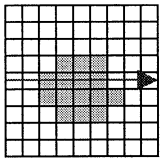
AMF : sliding AAF : 1000m^2	EMF : sliding EAF : 1150m^2	EMF : sliding EAF : 1200m^2	EMF : sliding EAF : 630m^2	EMF : sliding EAF : 1360m^2	EMF : sliding EAF : 1270m^2
	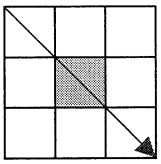	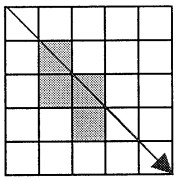	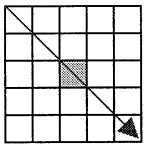	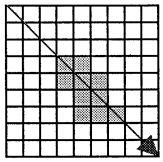	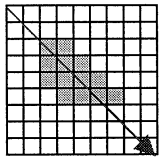
AMF : sliding AAF : 600m^2	EMF : sliding EAF : 910m^2	EMF : sliding EAF : 860m^2	EMF : sliding EAF : 370m^2	EMF : sliding EAF : 780m^2	EMF : sliding EAF : 800m^2
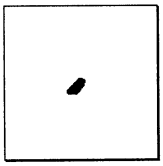	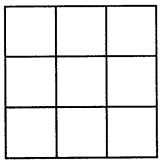	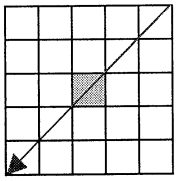	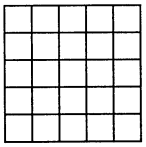	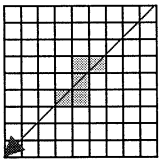	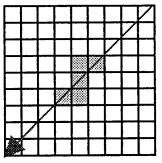
AMF : sliding AAF : 300m^2	EMF : unknown EAF : - m^2	EMF : sliding EAF : 370m^2	EMF : unknown EAF : - m^2	EMF : sliding EAF : 410m^2	EMF : sliding EAF : 420m^2

Figure 6. Mesh diagrams of case studies
Gray pixels are the area of estimated as slope failure
AMF: Actual Morphology of Failure, AAF: Actual Area of Failure
EMF: Estimated Morphology of Failure, EAF: Estimated Area of Failure

4 RESULTS

Figure 6 is mesh diagrams showing accuracies of the results. The actual failure shown in Figure 6 was surveyed using aerial photographs after the earthquake. In comparison with five cases, it is obvious that cases of using merged image are effective to detect the shape clearly. The distribution of the study area is shown in Figure 7. As shown in Table 2, the detection accuracies of five case studies, Case A, B, C, D and E, for the actual slope failure area of less than 900 square meters are about 40%, 90%, 20%, 100% and 100% respectively. The accuracy of over 900 square meters are almost 100% except Case is A and C. In comparison with the results of D and E(same resolution) for failures of less than 400 square meters, however, are 65% and 43% respectively.

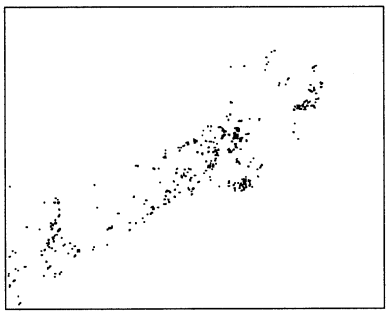

Result image of Case A
LANDSAT TM band5

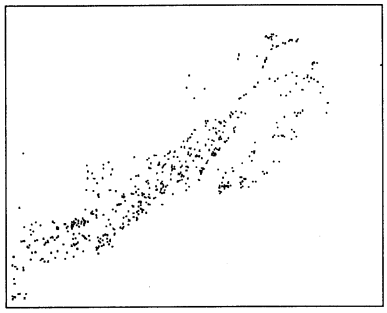

Result image of Case B
SPOT HRV-XS band 3

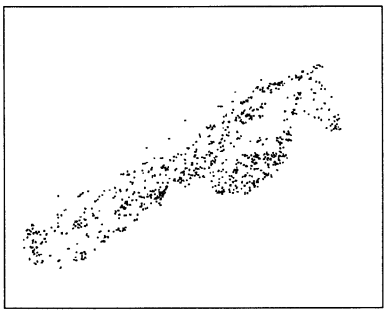

Result image of Case C
ADEOS AVNIR band 4

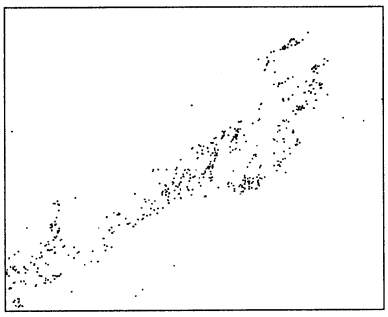

Result of Case D
10m-TM band 5

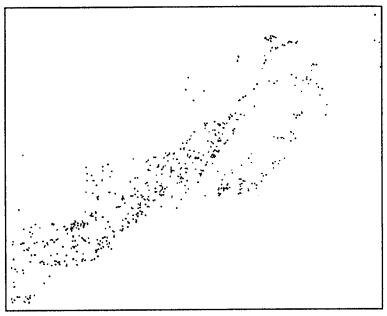

Result of Case E
10m-HRV-XS band 3

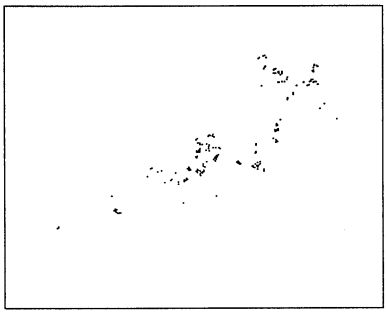

Actual distribution of slope failures
Surveyed by Okimura et al.

Figure 7. Result image of each case
Points: estimated(detected)/actual slope failures

Case	Used data	A.A.F(m^2) under 200		A.A.F(m^2) under 400		A.A.F(m^2) under 900		A.A.F(m^2) under 1800		A.A.F(m^2) over 1800	
Case 1	TM band 5	0		0		48	+	73	++	100	+++
Case 2	HRV-XS band 3	0		10		92	+++	100	+++	100	+++
Case 3	AVNIR band 4	8		10		26		50	+	100	+++
Case 4	10m-TM band 5	27		65	++	100	+++	100	+++	100	+++
Case 5	10m-HRV-XS band 3	17		43	+	100	+++	100	+++	100	+++

Table 2. Percent accuracies of case studies
A.A.F: Actual Area of Failure
+++(Very Good): over 80%, ++(Good): over 60%, +(Fair): over 40%, -(Poor): under 40%

5 CONCLUSIONS

This paper showed a morphological slope failure detector using satellite remote sensing data. From the results of five case studies, it was shown that the detector can detect the failures almost perfect for failures that size is over twice of actual one. In comparison with the results of using two different types(different wavelength) of merged images, originally low resolution data was more effective than originally high resolution one.

From the facts described above, we may conclude that it is important that not only the resolution but also the wavelength(particularly IR band) should be prepared for slope failures/landslides detection.

ACKNOWLEDGMENTS

Satellite data used in this study are provided by National Space Development Agency of Japan(NASDA). Slope failure maps is made by Prof. Okimura, Kobe University and aerial photographs are surveyed by ASIA KOSOKU co. ltd. At the end, the authors would like to expres their sincere gratitude.

REFERNENCES

Garguet, B., Girel, J., Chassery, J. and Pautou, G., 1996. The use of multiresolution analysis and wavelet transform for merging SPOT panchromatic and multispectral image data, Photogrametric Engineering & Remote sensing, Vol.62, No.9, pp.1057-1066.

Kawamura, M. and Tsujiko, Y., 1994. An approach to geographical pattern recognition using mathematical morphology, Proceedings of International Geoscience And Remote Sensing Symposium (IGARSS) '94.

Kawamura, M. and Tsujiko, Y., 1996. An application of multi-functional morphological operations to river edge detection for Landsat TM data, in Japanese, Journal of the Japan Society of Photogrammetry and Remote Sensing, Vol.35, No.5, pp.36-45.

Kawamura, M. and Tsujiko, Y., 1997. An application of morphology to monitoring of slope failure in Rokko mountain area using low resolution IR images, in Japanese, Journal of the Japan Society of Photogrammetry and Remote Sensing, Vol.36, No.4, pp.26-37.

Kawamura, M. and Tsujiko, Y., 1998. A detection method of morphological types and sizes for earthquake-induced slope failures using remote sensing data, in Japanese, Journal of the Japan Society of Civil Engineers, Vol.IV-40, No.597, pp.11-20.

Kawamura, M. and Tsujiko, Y., 1998. A GIS approach to the monitoring of damaged mountain slopes using satellite IR images, in Japanese, Journal of the Japan Society of Natural Disaster Science, Vol.17, No.3, pp.279-290.

Sassa, K., Fukuoka, H., Scarascia, G. and Evans, S., 1995. Earthquake-induced-landslides: distribution, motion and mechanism, Soils and Foundation, Special Issue on geotechnical aspects of the January 17 1995 Hyogoken-Nambu Earthquake, pp.53-64.

Tsujiko., Y., Kawamura, M. and Jayamanna, S., B., 1996. An edge detector based on wide-narrow morphological operations using remote sensing images, International archives of photogrammetry and remote sensing, Vol.XXXI, part B3(commission III), pp.886-889.

Yocky, D., A., 1996. Multiresolution wavelet decomposition image merger of LANDSAT Thematic Mapper and SPOT panchromatic data, Photogrametric Engineering & Remote sensing, Vol. 62, No. 9, pp.1067-1074.